INORGANIC CHEMISTRY FRONTIERS

RESEARCH ARTICLE

View Article Online
View Journal | View Issue

Cite this: *Inorg. Chem. Front.*, 2024, **11**, 4826

Single-component rare-earth-free white light-emitting metal–organic framework towards nitroaromatic explosive sensing and dye adsorption†

Yan-Wu Zhao, Bin Xue, Nan Zhang, Li-E Guo, Sheng-Yan Zhu and Xian-Ming Zhang *

Received 23rd March 2024,
Accepted 3rd June 2024

DOI: 10.1039/d4qi00747f

rsc.li/frontiers-inorganic

Given the current depletion of energy resources and the escalating severity of environmental issues, it is of utmost importance to develop sustainable materials capable of detecting harmful substances and removing adverse environmental impacts. Herein, a rare-earth-free white-light-emitting MOF Cd-PNMI (PNMI, *N*-(4-pyridyl)-1,4,5,8-naphathalene-tetracarboxy-monoimide), deriving from an idea that involves the construction of a strong white-light-emitting MOFs using a weak white-light-emitting ligand PNMI with d^{10} metal based on ligand-to-ligand charge transfer (LLCT) luminescent mechanism, was designed and confirmed using time-dependent density functional theory (TDDFT) calculations. As a sustainable white-light-emitting material, CdPNMI can not only detect explosive and highly toxic substances at low limits of detection (LOD) but also adsorb the dyes from waste liquids. The CdPNMI emulsion demonstrated ratiometric sensing with remarkable dual-emission fluorescence quenching for nitro explosive and highly toxic substances, which was confirmed to be the result of a synergetic contribution of photo-induced electronic transfer (PET) and Förster resonance energy transfer (FRET) quenching mechanism. Due to the distinctive structure character, CdPNMI also exhibited rapid, selective and extensive adsorption for Rhodamine B (RhB) and fluorescein (FITC) dye, contributing to the elimination of these pollutants from waste liquids.

Introduction

White light-emitting diodes (WLEDs), as the fourth generation green light source, have acquired increasing attention in the fields of display and lighting due to energy saving, long lifespan, environmental friendliness, and high luminous efficiency.[1,2] Among solid-state WLEDs, UV-WLEDs are regarded as the prospective directions.[3–7] As critical components of UV-WLEDs, white-light-emitting materials upon UV light excitation have become a research hotspot in recent years.[5,8,9] Especially, the white-light-emitting materials from vibrant luminescent MOFs offer a novel and different route from other materials because of their designed structures, tunable properties, and customizable functions by the judicious choice of metal nodes and organic linkers.[10,11] Luminescent MOFs originate from the three main luminescent centres of metal, ligand, and guest molecule.[12,13] White light MOFs are classified as multicomponent MOFs that are obtained from MOF pores encapsulated luminescent units (dyes, luminescent molecule, and lanthanide metal ions)[14–17] and single-component MOFs that are synthesized by adjusting the rare earth metal or transition metal with luminescent ligand.[18,19] However, multicomponent MOFs suffer from poor colour stability, low reproducibility, and chromatic aberration.[16] Therefore, developing single-component MOFs with white-light emission has emerged as a promising approach.[20] In view of the tight supply and escalating prices of non-renewable rare earth, it has become necessary to explore alternative non-rare-earth single-component white-light-emitting MOF materials.[21]

To date, the majority of the reported rare-earth-free white-light-emitting MOFs are multicomponent MOFs (guest encapsulated emitter);[13,16,22] however, single-component white-light MOFs are relatively scarce.[19,21,23] We have previously reported single-component white-light MOFs by doping different quan-

Key Laboratory of Magnetic Molecules & Magnetic Information Materials Ministry of Education, School of Chemistry & Material Science, Shanxi Normal University, Taiyuan, 030031 Shanxi, P. R. China. E-mail: zhangxm@dns.sxnu.edu.cn

†Electronic supplementary information (ESI) available: Experiment section, structure description and computation details, *etc*. CCDC 2336490. For ESI and crystallographic data in CIF or other electronic format see DOI: https://doi.org/10.1039/d4qi00747f

tities of Eu^{3+} (red light) and Tb^{3+} (green light) into blue-emitting MOFs based on trichromatic theory.[18] However, achieving rare-earth-free single-component white-light MOFs upon UV light excitation remains a considerable challenge due to the lack of effective adjustment strategies.

Herein, a feasible strategy is proposed to obtain rare-earth-free single-component white-light-emitting MOFs constructed using the weak white-light-emitting organic ligand with d^{10} metals. Indeed, the emission of luminescent MOFs comprised of d^{10} metals (*e.g.*, Zn and Cd) and fluorescent ligands typically involve ligand-based electron transfer or ligand-to-ligand charge transfer (LLCT) processes confirmed by recent studies.[24–26] Luminescent MOFs often show significantly enhanced photoluminescence (PL) with respect to the constituting ligands themselves, and the shift in emission energy is usually less than 15 nm compared to that of the ligand.[27,28] In order to create rare-earth-free, UV-excitable white-light-emitting MOFs, we aim to construct cadmium or zinc-based luminescent MOFs using white-light emissive ligands. Among various organic ligands, PNMI (*N*-(4-pyridyl)-1,4,5,8-naphthalenetetracarboxy-monoimide, Scheme S1†) have attracted our attention. The naphthalimides have a coplanar π-electron core and display potential photophysical properties, which can be advantageous to construct fluorescent MOFs. More importantly, PNMI emits weak white light with a relatively low quantum yield (Φ_f < 0.1%), rendering it an ideal linker candidate because the constructed MOFs can emit stronger white light.

As far as WLED is concerned, it is undoubtedly environmentally friendly. However, currently, the excess discharge of some pollutants such as nitroaromatic explosives and dyes has posed a serious threat to the environment and biological health.[29] How to detect and eliminate them is an urgent issue to be resolved. In recent years, the sensing applications of luminescent MOFs for detecting pollutants have been an extremely active area of research,[30] which is derived from their tunable and stable structures with large surface areas that can bring excellent selectivity, sensitivity, and recyclability.[31–33] The versatile MOFs constructed by naphthalimides are known to be a class of excellent candidates for sensors to detect nitroaromatic explosives such as 2,4,6-trinitrophenol (TNP), 4-nitrotoluene (4-NT), and nitrobenzene (NB) due to the abundant interactions and charge transfer between the host frameworks and the targeted guest molecules.[31] Up to now, the reported naphthalimide-based MOF sensors have mainly been focused on single-emission turn-off or turn-on fluorescent sensing.[34–38] However, the detection accuracy of single-signal MOF sensors is limited by various factors, including the solution concentration, instrument, environment, and excitation light intensity. The ratiometric fluorescence MOF sensors could eliminate these drawbacks through self-reference of dual emission, acquiring high-precision detection.[12] The constructed CdPNMI, as 3D porous MOFs, exhibits a remarkable porosity of 46% and features large pore sizes, along with abundant pyridyl-N and imide-O binding sites within the internal pore walls. Interestingly, the fluorescent titration experiments of CdPNMI emulsion by different concentrations of nitromatic explosives show a prominent dual-emission quenching effect. More distinctively, the constructing CdPNMI also displays amazing absorption for Rhodamine B (RhB) and fluorescein (FITC) dyes. Therefore, the Cd-based MOF in the work manifests multi-functional features with white light emission, fluorescent sensing, and dye absorption.

Experimental section

Materials and methods

Details on all materials and chemicals, the synthesis of organic compound DPNDI (*N*,*N*′-di-(4-pyridyl)-1,4,5,8-naphthalenete-tracarboxydiimide), PNMI and CdPNMI, the preparation of all solutions and measurements are supplied in the ESI,† and CCDC 2336490 contains the supplementary crystallographic data for this paper.†

Results and discussion

The organic ligand PNMI was synthesized by partial hydrolysis of DPNDI according to Scheme S1 (Fig. S1–S3).† CdPNMI was obtained with Cd salts and PNMI in a mixture of DMF and H_2O by a solvothermal method. Interestingly, it was accidentally found that CdPNMI can also be prepared DPNDI and Cd salts. The single-crystal structure contained a partially hydrolyzed product of DPNDI, which was consistent with the reported result.[39]

Single-crystal X-ray diffraction analysis reveals that CdPNMI crystallizes in the monoclinic $P2_1/n$ space group, which is isostructural with the [Cd(PNMI)]·0.5DMA·$5H_2O$ crystal.[39] The asymmetric unit includes one Cd(II) metal ion and one PNMI ligand. As depicted in Fig. 1, each Cd atom shows a six-co-

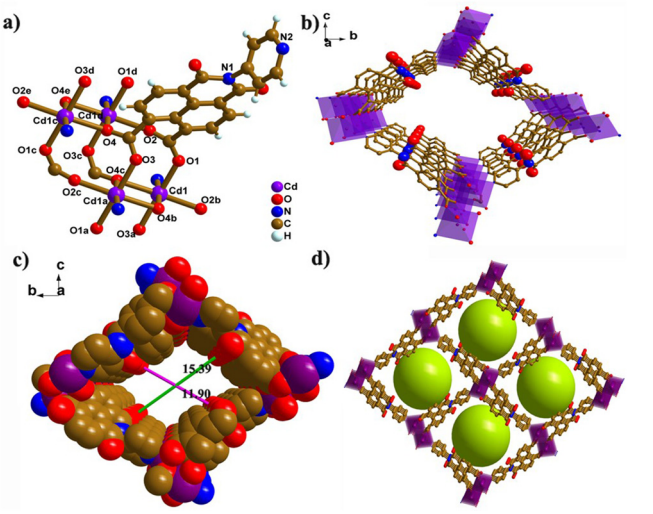

Fig. 1 Crystal structure of CdPNMI. (a) Representation of the Cd coordination environment; (b) 3D net with abundant nitrogen and oxygen sites along the inner channel walls; (c) space-filling model of a 1D channel viewed along the *a*-axis; (d) view of 1D channels along the *a* axis filled with green balls.

ordinated environment with a slightly distorted CdO_5N octahedral geometry (Fig. S4†). The Cd–O and Cd–N bond lengths are 2.213(3) to 2.347(3) Å and 2.277(3) to 2.278(3) Å, respectively. The L–Cd–L (L = N, O) bond angles range from 79.95(10) to 176.39(12)° and deviate slightly from those of the perfect octahedron (Tables S1 and S2†). Furthermore, a $Cd_2O_8N_2$ cluster is formed by two CdO_5N octahedrons with a shared side, which is derived from a rhomboid Cd_2O_2 ring generated by the two carboxylic O_4 atoms of two different ligands bridging two Cd atoms (Fig. 1a and Fig. S4b†). Each O_4 atom in the η^2 mode coordinates with the Cd atom, and the carboxylic group of the entire ligand in the μ_4-η^1:η^1:η^1:η^2 mode is coordinated to four Cd atoms (Fig. S4c†). The remaining three oxygen atoms are connected to another Cd_2O_2 ring, resulting in an extended 1D chain along the *a*-axis (Fig. S4d†). Four adjacent 1D chains are connected by Cd–N bonds of each ligand to form 3D MOFs with 1D channel (Fig. 1b–d). Topology analysis was conducted to further understand the 3D network, in which PNMI ligands and $Cd_2O_8N_2$ clusters are regarded as three-connected and six-connected nodes, respectively (Fig. S4e and f†). A calculation by TOPOS reveals a (3,6)-connected *rtl* network with a Schläfli point symbol of $(4{\cdot}6^2)2(4^2{\cdot}6^{10}{\cdot}8^3)$. The accessible pore void was obtained to be 46% of the total cell volume by the PLATON program. The 1D rhombus-like channels of CdPNMI had the interior cross-section dimensions of *ca.* 15.39 × 11.90 Å along the *a*-axis (subtracting the van der Waals radii of the two oxygen atoms, Fig. 1c).

X-ray photoelectron spectroscopy (XPS) was conducted to explore the elemental composition of the CdPNMI crystal. As depicted in Fig. S6,† the peaks of Cd, C, O and N are observed in the survey spectrum, confirming the presence of the above elements without impurities. The Cd 3d spectrum reveals two types of electron orbits, Cd $3d_{5/2}$ and Cd $3d_{3/2}$, at binding energies of 412.4 and 404.8 eV, respectively (Fig. 2a).[40,41] Different carbon environments are identified from the C 1s spectrum (Fig. 2b): three peaks at 284.8, 285.8 and 288.7 eV corresponding to C=C/C–C, C–N, and O=C–O bonds, respectively.[42]

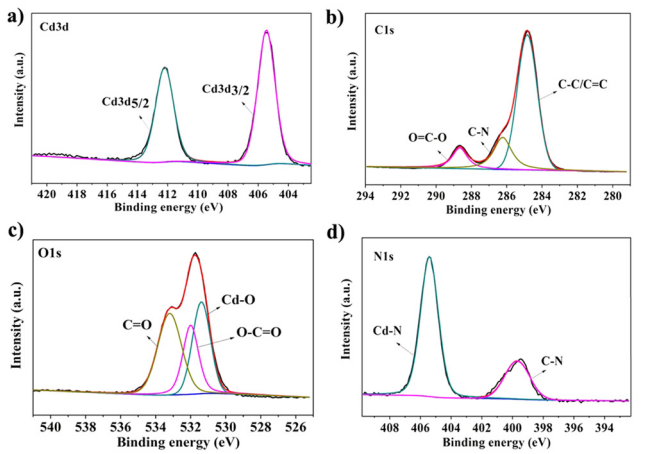

Fig. 2 XPS spectra of the CdPNMI crystal: (a) Cd 3d, (b) C 1s, (c) O 1s, and (d) N 1s.

Meanwhile, the peaks of O 1s at 531.4, 532.0, and 533.2 eV, are ascribed to Cd–O, O=C–O and O=C (amide) in Fig. 2c, respectively.[43] Fig. 2d shows the characteristic peaks of N 1s at 400.1 eV (C–N) and 404.8 eV (Cd–N).[41] In addition, IR spectra of CdPNMI describe the presence of the main functional group, further confirming the structure of CdPNMI (Fig. S3†). The PXRD analysis of CdPNMI, as depicted in Fig. S7,† shows close diffraction peaks with the simulated ones by single crystals, indicating the phase purity of the crystal. The morphology of the CdPNMI crystal is also investigated by scanning electron microscopy (SEM) images. As shown in Fig. S5,† CdPNMI crystal is composed of blocks and rods with smooth surfaces.

Similar PXRD of CdPNMI crystals immersed in different solvents indicated identical phases (Fig. S8†), suggesting the good solvent stability of CdPNMI. Meanwhile, thermogravimetric analysis of the CdPNMI crystal was performed at a temperature of 30–800 °C. The first weight loss in the range of 30–75 °C is attributed to the removal of water molecules from the crystal lattice. The second stage from 75 °C to 130 °C originates from the loss of guest water molecules. The decomposition of the organic ligand occurred at 320–436 °C (Fig. S12†), indicating that the CdPNMI crystal exhibited favorable thermostability.

CdPNMI showed a strong UV absorption band shifted to 260 nm and 370 nm (including 320 nm with the maximum absorption peak) compared with the transition peak of PNMI at 255 and 348 nm, corresponding to the $\pi \rightarrow \pi^*$ transition of PNMI ligands. In addition, a shoulder peak around 457 nm can be observed in CdPNMI, which could be attributed to an inter-molecular electron-transfer transition of the PNMI ligand (Fig. S13†).

The solid-state emission spectra of PNMI and CdPNMI were investigated under ambient conditions. As shown in Fig. 3a, PNMI ligands emit a weak white light and two broad bands with maximum emission at 446 and 541 nm under the excitation of 350 nm (Φ_f < 0.1%), which are assigned to $\pi \rightarrow \pi^*$ of intraligand and interligand electronic transitions (Fig. S27†). Compared with the PNMI ligands, the CdPNMI crystal emits significantly stronger white light and exhibits two broad bands with maximum emission at 440 and 548 nm under the excitation of 356 nm (Fig. 3b and Fig. S14†). The slight shift of the emission wavelength and broadening of the spectra are perhaps due to charge transfer among the organic ligands (LLCT) in the cyclically extending framework of CdPNMI. The CIE (Commission Internationale de l'Eclairage) coordinates for the emission of the PNMI ligand and CdPNMI crystal are calculated to be (0.295, 0.342) and (0.306, 0.331), all within the white region of the chromaticity graph (Fig. S15†). Interestingly, CdPNMI crystals can produce bright white light under different excitation light from 365 nm to 390 nm (Fig. S16†). As an important parameter, the fluorescence lifetime of the CdPNMI crystal was investigated, and the time-resolved PL lifetime measurements showed biexponential decays, with lifetimes of 3.06 ns and 5.25 ns, corresponding to the emission wavelength of 440 nm and 548 nm, respectively (Fig. 3c). The absolute fluorescence quantum yield (QY) of the

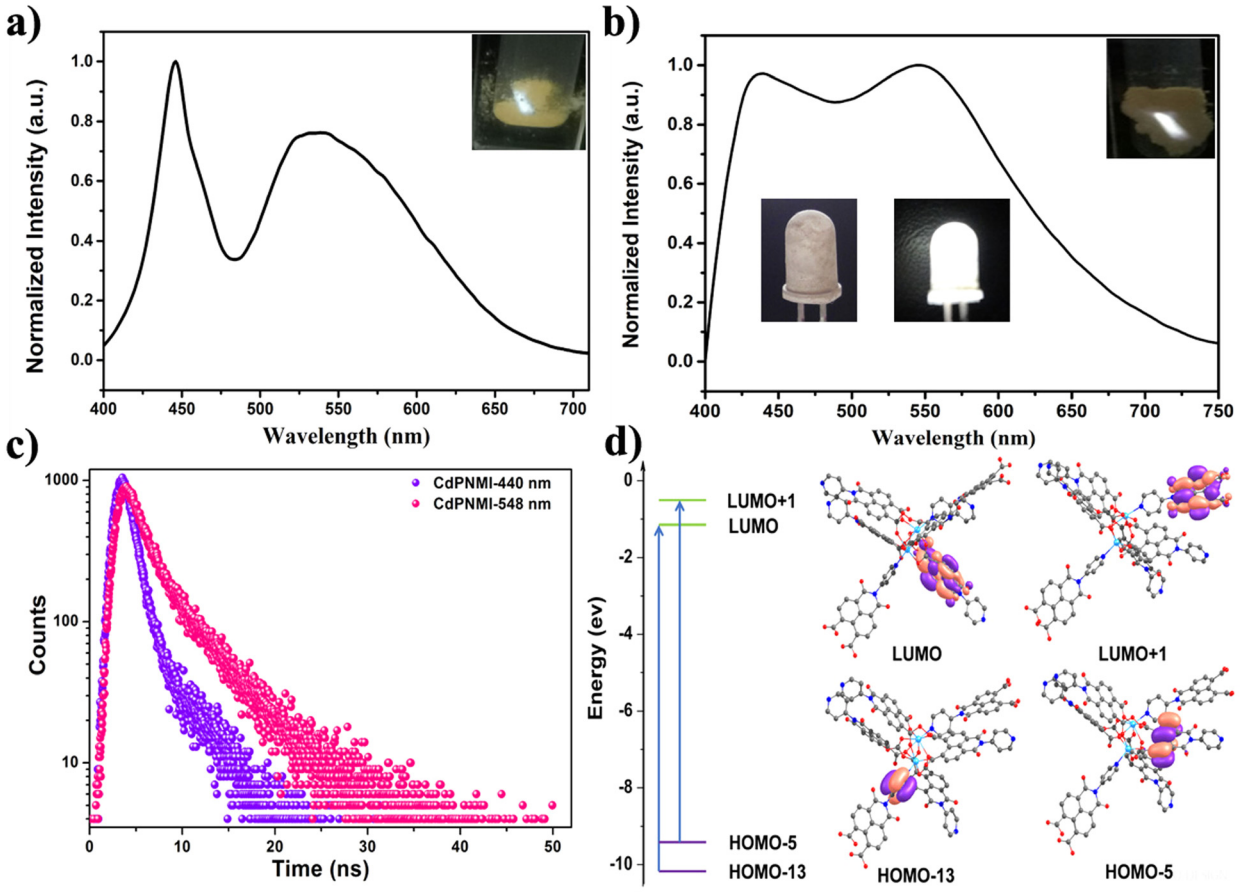

Fig. 3 Solid-state fluorescence spectra of the organic ligand PNMI (a) and CdPNMI (b). Inset: optical images of PNMI (a) and CdPNMI (b) under the maximum excitation, photographs of LEDs (b): a 3 mm reference UV LED (365 nm) coated with a thin layer of CdPNMI turned off (lower left) and turn on (lower right); (c) fluorescence decay profile of the CdPNMI crystal under different emission wavelengths (λ_{ex} = 356 nm); (d) energy transfer and computed frontier molecular orbitals of the CdPNMI model by the TDDFT method.

CdPNMI crystal was measured as 4.12% under 356 nm exciting with diffuse light within an integrating sphere. This means the fluorescence intensity is indeed enhanced by constructing the d^{10} metal MOFs with weak white-light-emitting PNMI ligand, confirming the feasibility of the design idea. Apparently, the rigid structure of the CdPNMI crystal confines the free movement of the PNMI ligand in the framework, resulting in the reduction of the nonradiative decay rate, further increasing the luminescent intensity and quantum efficiency.

To further confirm whether the luminescence mechanism in CdPNMI follows the ligand-to-ligand charge transfer (LLCT) or metal-to-ligand charge transfer (MLCT), TDDFT calculations were conducted. As depicted in Fig. 3d and Fig. S26,† the change of the electron cloud density distribution on the frontier orbitals of the CdPNMI model shows that an efficient charge transfer process could occur between the organic ligands. The calculated photophysical properties of CdPNMI are listed in Table S3.† All transitions show $\pi \rightarrow \pi^*$ transitions, and there are two local excitation states (S_{LE}) and four charge transfer states (S_{CT}). Interestingly, the two excited states exhibit a significant charge-transfer characteristic and are denoted as $S_{CT1}(\pi\pi^*)$ and $S_{CT3}(\pi\pi^*)$ with transition energies of 4.5295 and 4.6801 eV, respectively, corresponding to two large oscillator strengths (f = 0.7007 and 0.9280). The two primary types of transitions involve charge transfer (CT) from the pyridine ring of one ligand to the naphthalimide ring of the other ligand, and CT from the naphthalene ring of one ligand to the naphthalimide ring of the other ligand (Fig. 3d). The two varieties of the charge transfer process are the underlying cause of the dual-emission peak observed in CdPNMI. In fact, the fluorescence decay profile of CdPNMI for different emission wavelengths also suggests a different luminescent mechanism of the two emission peaks (Fig. 3c). This calculation verifies that the fluorescence of CdPNMI originates from LLCT, rather than MLCT.

Given that the CdPNMI crystal showed stronger white light under the excitation of 365 nm (Fig. S15†), the CdPNMI material was applied on a commercially available UV-LED lamp (Fig. 3b). Interestingly, the fabricated LED with a reported method emitted bright white light,[18] which indicated that the rare-earth-free MOFs CdPNMI constructed using the d^{10} metal exhibit favorable white-light properties.

In addition to the application of solid white lighting, CdPNMI also displayed a similar sensing ability to these reported naphthalene diimide MOF, especially for nitroaromatic compounds (NACs) with explosive pollutants and highly poisonous substances. Although several naphthalene diimide MOFs showed distinctive single-emission luminescent sensing,[35–38] few reports have appeared on similar dual-emission sensing.[44] The CdPNMI emulsion in DMA shows two emission peaks at 425 nm and 468 nm (Fig. S17†). To verify the sensing ability of CdPNMI towards a series of nitroaromatic explosives including TNP, NT, and NB, fluorescence titration experiments were carried out with gradual addition of NACs solutions to the CdPNMI emulsion. Interestingly, CdPNMI emulsion displayed remarkable dual-emission fluorescence quenching in the presence of these NACs (Fig. 4). Moreover, the decreasing degrees of the fluorescence intensity at 425 nm and 468 nm are different, and the experimental results show the decline of the emission peak at 425 nm are faster than that at 468 nm, which belongs to ratiometric fluorescence sensing with the same change of the two emissions in different varying degrees.[12] Given that CdPNMI shows two emission peaks due to different LLCT pathways, these analytes (NACs) partly interdict LLCT, which may further affect the descent degree of fluorescence intensity of two emissions. For the sensing of TNP, the fluorescence intensity at 425 nm is reduced to 57.4% of the original level by adding 29.4 μM of TNP into the CdPNMI emulsion, whereas the fluorescence intensity at 468 nm decreases to 42.3% of its initial intensity. Similarly, the 22.6% and 16.6% fluorescence quenching at 425 nm and 468 nm were observed by adding 29.4 μM of 4-NT (Fig. S19†), and the addition of 29.4 μM of NB results in the 23.6% and 18.5% fluorescence quenching at 425 nm and 468 nm, respectively (Fig. S18†). Among all the nitro explosives, TNP exhibits the highest quenching efficiency of the emission intensity of CdPNMI (Fig. 4a and Fig. S18, S19†). In addition, high-poisonous 4-nitro aniline (4-NA) was attempted as a probed nitroaromatic compound. Surprisingly, the CdPNMI emulsion shows conspicuous fluorescence quenching and is almost completely quenched upon the addition of 114 μM of 4-NA, which is nearly the same as the quenching efficiency of TNP. Likewise, the addition of 29.4 μM of 4-NA caused 54.6% and 43.6% fluorescence quenching at 425 nm and 468 nm, respectively. A detailed analysis of fluorescence quenching for TNP and 4-NA was conducted. As shown in Fig. S20 and S21,† the different fluorescence quenching by TNP and NA follow the nonlinear behavior in the concentration range of 0–114 μM, which is fitted by the empirical equation of $I/I_0 = 1 + a \times \exp(K[Q])$. Based upon the above

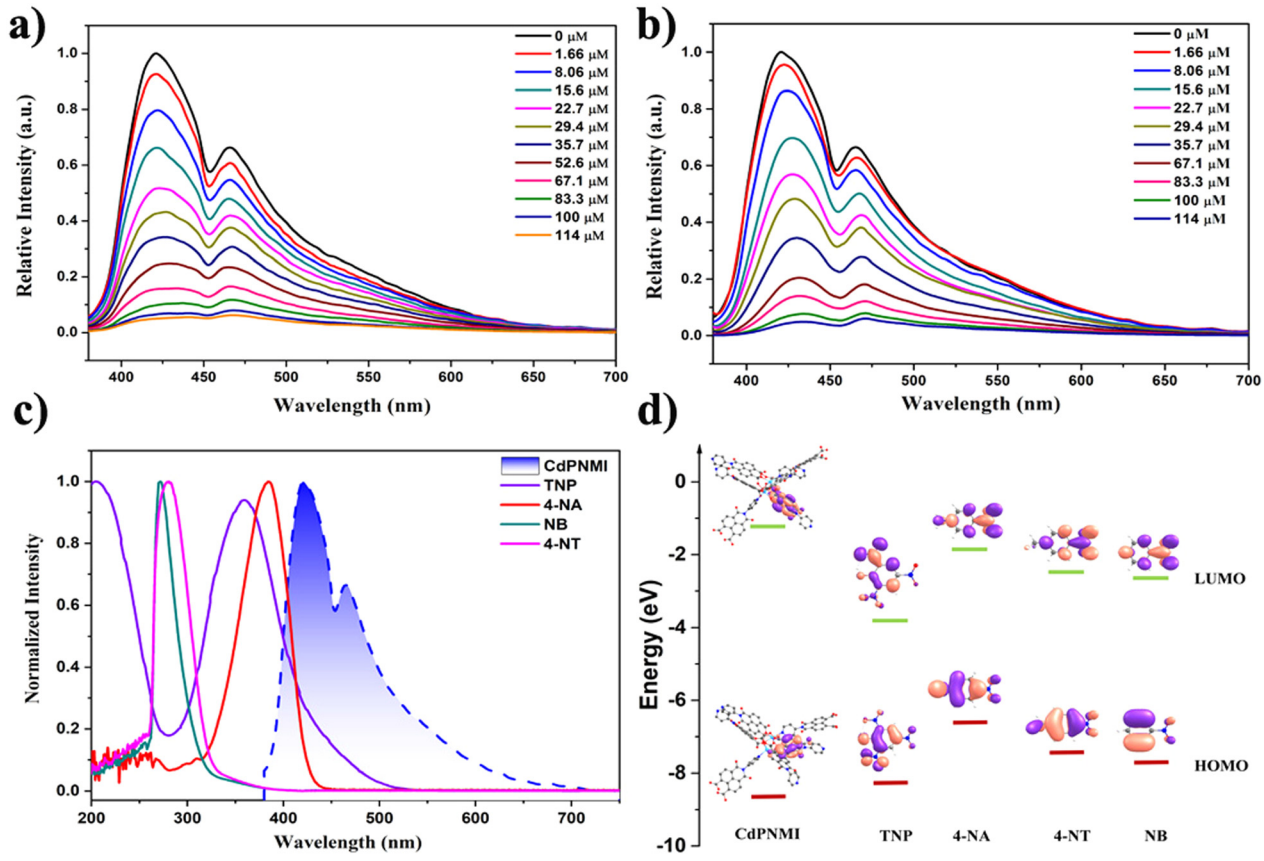

Fig. 4 Changes in the emission intensity of CdPNMI emulsion upon incremental additions of (a) TNP and (b) 4-NA; (c) spectral overlap between the normalized absorption spectra of NACs with the normalized emission spectrum of CdPNMI; (d) HOMO and LUMO energy levels of CdPNMI and nitro aromatic compounds.

fitting results, a linear quenching plot was acquired, and their quenching constants (K_{SV}) are 4.4×10^4 and 3.8×10^4, respectively.[45] The limit of detection (LOD) for TNP was estimated to be 0.42 ppm, which was a lower value,[46] and the LOD of NA was 0.49 ppm, which were calculated according to the 3σ criteria. The high value of K_{SV} and low LOD indicates the high sensitivity of CdPNM for the detection of TNP over other nitro analytes.

To verify the reusability of CdPNMI sensing for TNP, cycling experiments were conducted for TNP detections. As shown in Fig. S22,† CdPNMI exhibits excellent regenerative stability to TNP. After five cycles, the fluorescent intensities and quenching efficiencies of CdPNMI only exhibited slight decreases. More importantly, the PXRD of CdPNMI crystal retains the original structure in Fig. S9,† indicating the good stability of CdPNMI. Meanwhile, the anti-interference experiments were also carried out. The selective sensing ability of CdPNMI for TNP was not disturbed by toluene (PhMe), NB, and 4-NT competitors (Fig. S23 and S24†). High selectivity, stability, and reusing capability endow CdPNMI with the potential for subsequent practical applications.

The fluorescence quenching mechanism needs to be further explored for interpreting the aforementioned experimental results. As shown in Fig. S25,† the Stern–Volmer plot of TNP and 4-NA shows linear growth at low concentrations and an upward curve with increasing concentrations, however, that of NB and 4-NT display a linear change. The nonlinear trends indicate the energy transfer between CdPNMI and TNP, which may be caused by static and dynamic quenching mechanisms. The static quenching mechanism can be due to a ground-state and non-fluorescent complex formed by analytes diffusing into the pores of CdPNMI. Dynamic quenching can relate to photo-induced electronic transfer (PET) and Förster resonance energy transfer (FRET). To further confirm the PET mechanism, a DFT calculation was executed for the HOMO–LUMO energy level of analytes. As depicted in Fig. 4d, the LUMO energy level of CdPNMI is obviously higher than that of the probed NACs, which means photo-induced electron transfer from the CdPNMI framework to the electron-deficient NACs. It is well known that the lower the LUMO level of analytes, the easier the electron transfer. For the probed NACs, the order of their LUMO level is 4-NA > 4-NT > NB > TNP, so TNP has the highest fluorescence quenching efficiency among all the probed NACs. Although the LUMO level of 4-NT and NB is lower than that of 4-NA, the experiment results display that the quenching efficiency of 4-NA is clearly higher, which indicates that there lies another quenching mechanism. From Fig. 4c it can be seen that the UV absorption spectra of TNP and 4-NA partly overlap with the emission spectra of the CdPNMI emulsion, suggesting energy transfer from CdPNMI from its excited state to NACs. This is a typical FRET mechanism. In general, the more the spectral overlap between the UV absorbance spectra of NACs and the emission spectra of MOF, the greater the chance of energy transfer and therefore higher fluorescence quenching. Therefore, TNP displays the highest quenching efficiency, and there is not much difference between TNP and 4-NA. For NB and 4-NT, there lies no FRET mechanism. In conclusion, the combination of PET and FRET mechanisms explicitly supports the fluorescence quenching of these NACs.

In recent years, the widespread utilization of some synthetic organic dyes, including Rhodamine B (RhB) and fluorescein (FITC), has resulted in their elevated discharge into the environment, posing a significant threat to life and the environment due to their toxic nature at higher concentrations.[47,48] Procedures utilized for dye removal from the environment encompass membrane filtration, biological treatment, and adsorption.[49] Among these, adsorption is the most widely used technique for dye remediation in the environment, attributed to its efficacy and impressive color removal capabilities. The advent of MOFs can be an excellent candidate because of their adjustable porous structure and designable and modifiable functionality.[50] However, the promising research on the removal of dyes from waste liquid using MOFs has received less attention. In view of the structural characteristics of CdPNMI with 46% porosity and the abundant N and O sites in the pores, CdPNMI may exhibit a certain dye absorption ability. Due to the pore size of 15.39×11.90 Å, the confinement effect of CdPNMI pores results in the selection of the dye molecules with the fit size. Rhodamine B and fluorescein possess sizes of 15.8×10.4 Å and 13.1×11.2 Å, respectively (Fig. S28†). Therefore, these two dyes were selected as adsorbates.

The CdPNMI crystals (each 5 mg) were individually added to different concentrations of RhB or FITC in 20 mL acetone solution. The solution was shaken, and allowed to stand. Subsequently, the UV-vis spectra of the solution were measured according to the duration of shaking. As shown in Fig. 5, UV-vis spectra display that CdPNMI crystals rapidly adsorb near 70% FITC dyes in 2 minutes, whereas only 60% RhB dye was adsorbed at the same time, and after 4 h, reaching complete absorption. Obviously, the rate and dose of FITC absorption are faster and more than those for RhB absorption, which indicates that CdPNMI exhibits not only the selective absorption capability of these dyes but also the potential for rapid absorption applications.

To precisely quantify the dye uptake capacities of CdPNMI, an equal amount of adsorbents (5 mg) was added to different

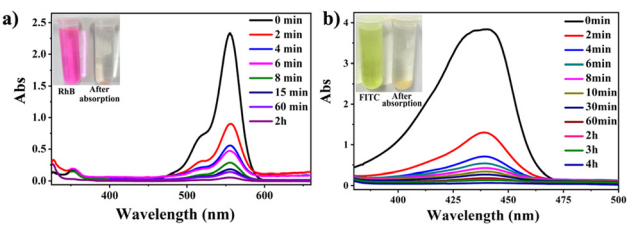

Fig. 5 Temporal evolution of UV/Vis absorption spectra of 20 mL acetone solution containing (a) RhB (20 mg L^{-1}), (b) FITC (550 mg L^{-1}) for CdPNMI adsorption. The photographs show the colours of the solution and crystal before and after organic dye adsorption.

concentrations of the organic dyes RhB (from 5 mg L^{-1} to 100 mg L^{-1}) or FITC (from 50 mg L^{-1} to 550 mg L^{-1}) in 20 mL acetone. UV-vis spectra were used to monitor the uptake capacity of CdPNMI (Fig. S29†). The adsorbent dosage for the adsorption process was determined, and the absorbance before and after the adsorption process was measured to calculate the quantity (q_e) of RhB (64 mg g^{-1}) and FITC (1000 mg g^{-1}) adsorbed at the equilibrium (ESI†). To our knowledge, the uptake capacity of FITC by CdPNMI is the highest among all of the reported absorption materials (Table S4†), although CdPNMI is a neutral network. Meanwhile, the PXRDs of CdPNMI crystal after adsorbing different concentrations of RhB or FITC in acetone solution were measured, which essentially showed the intact structure, as shown in Fig. S10 and S11,† further confirming the stability of the CdPNMI crystal.

The absorption difference between RhB and FITC dyes motivated us to explore the absorption mechanism. First, from the size confinement, FITC molecules could be easier to accommodate into the 1D pores of CdPNMI compared to the RhB molecules; secondly, the carboxyl group of RhB and two hydroxyl and carbonyl groups of FITC can generate hydrogen bonds with the exposed oxygen of the carbonyl group in CdPNMI pores, leading to the enlargement of adsorption. As shown in Fig. 6, IR spectra of RhB@CdPNMI and FITC@CdPNMI show peaks of CdPNMI and dyes, suggesting these dyes are completely encompassed by the CdPNMI crystal. The peak of RhB@CdPNMI at 3411 cm^{-1}, derived from the 3446 cm^{-1} peak of RhB, is attributed to the O–H stretching vibration of –COOH in RhB. Upon absorption of the RhB molecules, the peak position of CdPNMI undergoes a shift towards the lower wavenumber, accompanied by a broadening effect. Meanwhile, the peak of CdPNMI at 1669 cm^{-1} shifts to 1663 cm^{-1} in RhB@CdPNMI, which is ascribed to the vibration peak of C═O, along with the increase of peak intensity. These peak changes suggest the existence of a hydrogen bond between the C═O of CdPNMI and –COOH of RhB. Similarly, for FITC@CdPNMI, the change of the 3426 cm^{-1} peak of the hydroxyl group and the 1659 cm^{-1} peak of the carbonyl group can show the presence of hydrogen bonds between the two groups. Furthermore, the more the formed hydrogen bonds, the stronger the interaction of CdPNMI and dyes, resulting in an increasing absorption dosage of CdPNMI for dyes. This is consistent with our experimental conclusions.

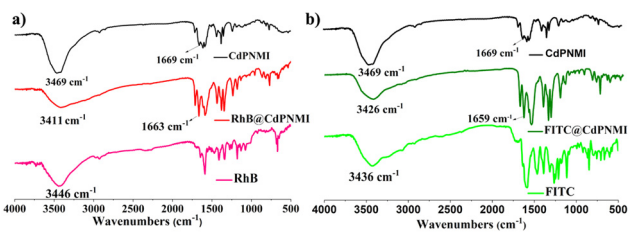

Fig. 6 IR spectra of RhB (a) and FITC (b) dyes before and after absorption of CdPNMI.

Conclusions

In conclusion, a single-component rare-earth-free white-light-emitting MOFs (CdPNMI) was developed based on a designable concept that is a strong white-light-emitting MOFs constructed by a weak white-light emissive ligand (PNMI) with d^{10} metal. Impressively, CdPNMI emits a bright white light (QY) under different exciting wavelengths of 365–390 nm, and a WLED was fabricated by utilizing CdPNMI on a commercially available UV-LED lamp. TDDFT calculation indicated the LLCT mechanism, excluding the possibility of MLCT. As a luminescent material, CdPNMI also demonstrated remarkable detective capabilities for nitroexplosive and highly toxic substances. Different from the reported single-emission MOF sensors based on a naphthalene diimide ligand, the CdPNMI emulsion in DMA displayed ratiometric sensing with dual-emission fluorescence quenching. The explosive TNP and high toxic 4-NA almost completely quenched the emission of CdPNMI emulsion, and the LODs for TNP and 4-NA were 0.42 ppm and 0.49 ppm, respectively. The quenching mechanism was confirmed to be the result of a combination of PET and FRET from DFT calculations and experiment validations. Meanwhile, CdPNMI presents rapid, selective and large absorption capacity for RhB (64 mg g^{-1}) and FITC (1000 mg g^{-1}) dyes, which are mainly derived from the distinctive structure of CdPNMI. The absorption mechanism can be illustrated by the confinement effect of the CdPNMI pores and the strong hydrogen-bonding interaction between dye molecules and the carbonyl group in the wall of the hole. The utilization of CdPNMI for the absorption of RhB and FITC will significantly contribute to the elimination of these pollutants from waste liquids. Overall, the versatile CdPNMI demonstrates remarkable properties in white light, ratiometric fluorescence sensing, and dye absorption.

Author contributions

The manuscript was written through the contributions of all authors. All authors have given their approval to the final version of the manuscript.

Conflicts of interest

There are no conflicts to declare.

Acknowledgements

This work was supported by the Natural Science Foundation of Shanxi Province (20210302124253).

References

1 J. Chen, J. Wang, X. Xu, J. Li, J. Song, S. Lan, S. Liu, B. Cai, B. Han, J. T. Precht, D. Ginger and H. Zeng, Efficient and

bright white light-emitting diodes based on single-layer heterophase halide perovskites, *Nat. Photonics*, 2021, **15**, 238–244.

2 L. Wang, R.-J. Xie, Y. Li, X. Wang, C.-G. Ma, D. Luo, T. Takeda, Y.-T. Tsai, R.-S. Liu and N. Hirosaki, $Ca_{1-x}Li_xAl_{1-x}Si_{1+x}N_3:Eu^{2+}$ solid solutions as broadband, color-tunable and thermally robust red phosphors for superior color rendition white light-emitting diodes, *Light: Sci. Appl.*, 2016, **5**, e16155.

3 J. Luo, X. Wang, S. Li, J. Liu, Y. Guo, G. Niu, L. Yao, Y. Fu, L. Gao, Q. Dong, C. Zhao, M. Leng, F. Ma, W. Liang, L. Wang, S. Jin, J. Han, L. Zhang, J. Etheridge, J. Wang, Y. Yan, E. H. Sargent and J. Tang, Efficient and stable emission of warm-white light from lead-free halide double perovskites, *Nature*, 2018, **563**, 541–545.

4 Y. Wei, G. Xing, K. Liu, G. Li, P. Dang, S. Liang, M. Liu, Z. Cheng, D. Jin and J. Lin, New strategy for designing orangish-red-emitting phosphor via oxygen-vacancy-induced electronic localization, *Light: Sci. Appl.*, 2019, **8**, 15.

5 Z. Ma, Z. Shi, D. Yang, Y. Li, F. Zhang, L. Wang, X. Chen, D. Wu, Y. Tian, Y. Zhang, L. Zhang, X. Li and C. Shan, High Color-Rendering Index and Stable White Light-Emitting Diodes by Assembling Two Broadband Emissive Self-Trapped Excitons, *Adv. Mater.*, 2021, **33**, 2001367.

6 H. Dalal, M. Kumar, S. Kaushik, P. Sehrawat, M. Sheoran, N. Sehrawat and R. K. Malik, Crystal Phase Recognition and Photoluminescence Behavior of Deep Reddish-Orange Sm^{3+}-Activated $Ca_9Gd(VO_4)_7$ Nanocrystals for Modern Solid-State Lightings, *J. Electron. Mater.*, 2023, **52**, 2780–2793.

7 H. Su, H. Lin, P. Li, B. Li, X. Xu, J. Li, Y. Wu, J. Hui and D. Liu, Conversion of Waste Expanded Polystyrene into Blue-Emitting Polymer Film for Light-Emitting Diode Applications, *Polymers*, 2023, **15**, 4693.

8 T. Yuan, F. Yuan, X. Li, Y. Li, L. Fan and S. Yang, Fluorescence–phosphorescence dual emissive carbon nitride quantum dots show 25% white emission efficiency enabling single-component WLEDs, *Chem. Sci.*, 2019, **10**, 9801–9806.

9 J.-H. Wei, J.-F. Liao, L. Zhou, J.-B. Luo, X.-D. Wang and D.-B. Kuang, Indium-antimony-halide single crystals for high-efficiency white-light emission and anti-counterfeiting, *Sci. Adv.*, 2021, **7**, eabg3989.

10 R. Haldar, L. Heinke and C. Wöll, Advanced Photoresponsive Materials Using the Metal–Organic Framework Approach, *Adv. Mater.*, 2020, **32**, 1905227.

11 Q. Wang, Q. Liu, X.-M. Du, B. Zhao, Y. Li and W.-J. Ruan, A white-light-emitting single MOF sensor-based array for berberine homologue discrimination, *J. Mater. Chem. C*, 2020, **8**, 1433–1439.

12 L. Chen, D. Liu, J. Peng, Q. Du and H. He, Ratiometric fluorescence sensing of metal-organic frameworks: Tactics and perspectives, *Coord. Chem. Rev.*, 2020, **404**, 213113.

13 N.-C. Chiu, K. T. Smith and K. C. Stylianou, Metal-Organic Frameworks for white light emission: From synthesis to device fabrication, *Coord. Chem. Rev.*, 2022, **459**, 214441.

14 W. P. Lustig and J. Li, Luminescent Metal-Organic Frameworks and coordination polymers as alternative phosphors for energy efficient lighting devices, *Coord. Chem. Rev.*, 2018, **373**, 116–147.

15 M. Li, G. Ren, W. Yang, Y. Yang, W. Yang, Y. Gao, P. Qiu and Q. Pan, Dual-emitting piezofluorochromic dye@MOF for white-light generation, *Chem. Commun.*, 2021, **57**, 1340–1343.

16 Y. Wen, T. Sheng, X. Zhu, C. Zhuo, S. Su, H. Li, S. Hu, Q.-L. Zhu and X. Wu, Introduction of Red-Green-Blue Fluorescent Dyes into a Metal-Organic Framework for Tunable White Light Emission, *Adv. Mater.*, 2017, **29**, 1700778.

17 C.-Y. Sun, X.-L. Wang, X. Zhang, C. Qin, P. Li, Z.-M. Su, D.-X. Zhu, G.-G. Shan, K.-Z. Shao, H. Wu and J. Li, Efficient and tunable white-light emission of Metal–Organic Frameworks by iridium-complex encapsulation, *Nat. Commun.*, 2013, **4**, 2717.

18 Y.-W. Zhao, F.-Q. Zhang and X.-M. Zhang, Single Component Lanthanide Hybrids Based on Metal–Organic Framework for Near-Ultraviolet White Light LED, *ACS Appl. Mater. Interfaces*, 2016, **8**, 24123–24130.

19 C. Peng, X. Song, J. Yin, G. Zhang and H. Fei, Intrinsic White-Light-Emitting Metal–Organic Frameworks with Structurally Deformable Secondary Building Units, *Angew. Chem., Int. Ed.*, 2019, **58**, 7818–7822.

20 M.-S. Wang and G.-C. Guo, Inorganic–organic hybrid white light phosphors, *Chem. Commun.*, 2016, **52**, 13194–13204.

21 T. Mondal, S. Mondal, S. Bose, D. Sengupta, U. K. Ghorai and S. K. Saha, Pure white light emission from a rare earth-free intrinsic Metal-Organic Framework and its application in a WLED, *J. Mater. Chem. C*, 2018, **6**, 614–621.

22 J.-C. Yin, Z. Chang, N. Li, J. He, Z.-X. Fu and X.-H. Bu, Efficient Regulation of Energy Transfer in a Multicomponent Dye-Loaded MOF for White-Light Emission Tuning, *ACS Appl. Mater. Interfaces*, 2020, **12**, 51589–51597.

23 C. Wang, Z. Yin, W.-M. Ma, X.-Y. Li, L.-H. Cao, Y. Cheng, X.-Y. Yu and Y.-M. Ma, Near sunlight continuous broadband white-light emission by single-phase Zn(II)-1,3,5-benzenetricarboxylate MOFs, *Dalton Trans.*, 2019, **48**, 14966–14970.

24 S. Bej, R. Das, N. C. Murmu and P. Banerjee, Selective Identification and Encapsulation of Biohazardous m-Xylene among a Pool of Its Other Constitutional C_8 Alkyl Isomers by Luminescent d^{10} MOFs: A Combined Theoretical and Experimental Study, *Inorg. Chem.*, 2020, **59**, 4366–4376.

25 Y.-H. He, Y.-L. Feng, Y.-Z. Lan and Y.-H. Wen, Syntheses, Structures, and Photoluminescence of Four d^{10} Metal–Organic Frameworks Constructed from 3,5-Bis-oxyacetate-benzoic Acid, *Cryst. Growth Des.*, 2008, **8**, 3586–3594.

26 S. Pramanik, C. Zheng, X. Zhang, T. J. Emge and J. Li, New Microporous Metal–Organic Framework Demonstrating Unique Selectivity for Detection of High Explosives and Aromatic Compounds, *J. Am. Chem. Soc.*, 2011, **133**, 4153–4155.

27 P. L. Feng, J. J. I. V. Perry, S. Nikodemski, B. W. Jacobs, S. T. Meek and M. D. Allendorf, Assessing the Purity of Metal–Organic Frameworks Using Photoluminescence: MOF-5, ZnO Quantum Dots, and Framework Decomposition, *J. Am. Chem. Soc.*, 2010, **132**, 15487–15489.
28 C. Zhang, Y. Che, Z. Zhang, X. Yang and L. Zang, Fluorescent nanoscale zinc(II)-carboxylate coordination polymers for explosive sensing, *Chem. Commun.*, 2011, **47**, 2336–2338.
29 J. H. Song and D. W. Kang, Hazardous nitroaromatic explosives detection by emerging porous solid sensors, *Coord. Chem. Rev.*, 2023, **492**, 215279.
30 T. Wang, Y. Jia, Q. Chen, R. Feng, S. Tian, T.-L. Hu and X.-H. Bu, A new luminescent metal-organic framework for selective sensing of nitroaromatic explosives, *Sci. China: Chem.*, 2016, **59**, 959–964.
31 T. Rasheed and F. Nabeel, Luminescent Metal-Organic Frameworks as potential sensory materials for various environmental toxic agents, *Coord. Chem. Rev.*, 2019, **401**, 213065.
32 X. Wang, Y. Jiang, A. Tissot and C. Serre, Luminescent sensing platforms based on lanthanide Metal-Organic Frameworks: Current strategies and perspectives, *Coord. Chem. Rev.*, 2023, **497**, 215454.
33 W. P. Lustig, S. Mukherjee, N. D. Rudd, A. V. Desai, J. Li and S. K. Ghosh, Metal–Organic Frameworks: functional luminescent and photonic materials for sensing applications, *Chem. Soc. Rev.*, 2017, **46**, 3242–3285.
34 L. Qin, H. Ma, M. Lv, Y. Zhou and L. Han, A naphthalenediimide-based Cd-MOF as solvatochromic sensor to detect organic amines, *J. Solid State Chem.*, 2023, **317**, 123660.
35 S. S. Dhankhar, N. Sharma and C. M. Nagaraja, Construction of bifunctional 2-fold interpenetrated Zn(II) MOFs exhibiting selective CO_2 adsorption and aqueous-phase sensing of 2,4,6-trinitrophenol, *Inorg. Chem. Front.*, 2019, **6**, 1058–1067.
36 J.-J. Liu, Y.-B. Shan, C.-R. Fan, M.-J. Lin, C.-C. Huang and W.-X. Dai, Encapsulating Naphthalene in an Electron-Deficient MOF to Enhance Fluorescence for Organic Amines Sensing, *Inorg. Chem.*, 2016, **55**, 3680–3684.
37 A. Mallick, B. Garai, M. A. Addicoat, P. S. Petkov, T. Heine and R. Banerjee, Solid state organic amine detection in a photochromic porous metal organic framework, *Chem. Sci.*, 2015, **6**, 1420–1425.
38 Y. Zhou and L. Han, Recent advances in naphthalenediimide-based Metal-Organic Frameworks: Structures and applications, *Coord. Chem. Rev.*, 2021, **430**, 213665.
39 R. Medishetty, D. Jung, X. Song, D. Kim, S. S. Lee, M. S. Lah and J. J. Vittal, Solvent-Induced Structural Dynamics in Noninterpenetrating Porous Coordination Polymeric Networks, *Inorg. Chem.*, 2013, **52**, 2951–2957.
40 Y. Zhang, Y. Liu, P. G. Karmaker, L. Zhang, K. Yang, L. Chen and X. Yang, Fabrication of Two Luminescent Imidazolyl Cadmium-Organic Frameworks and Their Sensing Mechanism for 2,6-Dichloro-4-nitroaniline, *ACS Appl. Mater. Interfaces*, 2023, **15**, 6177–6186.
41 C. Fan, B. Zhu, X. Zhang, C. Bi, D. Zhang, Z. Zong and Y. Fan, Highly Stable Acid-Induced Emission-Enhancing Cd-MOFs: Synthesis, Characterization, and Detection of Glutamic Acid in Water and Fe Ions in Acid, *Inorg. Chem.*, 2021, **60**, 6339–6348.
42 Q.-Q. Liu, K.-F. Yue, X.-J. Weng and Y.-Y. Wang, Luminescence sensing and supercapacitor performances of a new (3,3)-connected Cd-MOF, *CrystEngComm*, 2019, **21**, 6186–6195.
43 Z.-X. Li, X. Zhang, Y.-C. Liu, K.-Y. Zou and M.-L. Yue, Controlling the BET Surface Area of Porous Carbon by Using the Cd/C Ratio of a Cd–MOF Precursor and Enhancing the Capacitance by Activation with KOH, *Chem. – Eur. J.*, 2016, **22**, 17734–17747.
44 R. Huo, C. Wang, M. Y. Wang, M. Y. Sun, S. Jiang, Y. H. Xing and F. Y. Bai, Preparation of Naphthalenediimide-Decorated Electron-Deficient Photochromic Lanthanide (III)-MOF and Paper Strip as Multifunctional Recognition and Ratiometric Luminescent Turn-On Sensors for Amines and Pesticides, *Inorg. Chem.*, 2023, **62**, 6661–6673.
45 E.-L. Zhou, P. Huang, C. Qin, K.-Z. Shao and Z.-M. Su, A stable luminescent anionic porous metal–organic framework for moderate adsorption of CO_2 and selective detection of nitro explosives, *J. Mater. Chem. A*, 2015, **3**, 7224–7228.
46 G. Radha, T. Leelasree, D. Muthukumar, R. S. Pillai and H. Aggarwal, Highly selective detection of TNP over other nitro compounds in water: the role of selective host–guest interactions in Zr-NDI MOF, *New J. Chem.*, 2021, **45**, 12931–12937.
47 W. Yan, L.-J. Han, H.-L. Jia, K. Shen, T. Wang and H.-G. Zheng, Three Highly Stable Cobalt MOFs Based on "Y"-Shaped Carboxylic Acid: Synthesis and Absorption of Anionic Dyes, *Inorg. Chem.*, 2016, **55**, 8816–8821.
48 Q. Li, Z.-L. Fan, D.-X. Xue, Y.-F. Zhang, Z.-H. Zhang, Q. Wang, H.-M. Sun, Z. Gao and J. Bai, A multi-dye@MOF composite boosts highly efficient photodegradation of an ultra-stubborn dye reactive blue 21 under visible-light irradiation, *J. Mater. Chem. A*, 2018, **6**, 2148–2156.
49 L. Liu, X.-N. Zhang, Z.-B. Han, M.-L. Gao, X.-M. Cao and S.-M. Wang, An In^{III}-based anionic metal–organic framework: sensitization of lanthanide(III) ions and selective absorption and separation of cationic dyes, *J. Mater. Chem. A*, 2015, **3**, 14157–14164.
50 D. Jiang, M. Chen, H. Wang, G. Zeng, D. Huang, M. Cheng, Y. Liu, W. Xue and Z. Wang, The application of different typological and structural MOFs-based materials for the dyes adsorption, *Coord. Chem. Rev.*, 2019, **380**, 471–483.

